Laser-Rewriteable Ferromagnetism at Thin-Film Surfaces

Jonathan Ehrler,[†,‡] Miao He,[§] Maxim V. Shugaev,[§] Nikolay I. Polushkin,[∥,⊥] Sebastian Wintz,[†,#] Vico Liersch,[†] Steffen Cornelius,[†] René Hübner,[†] Kay Potzger,[†] Jürgen Lindner,[†] Jürgen Fassbender,[†,‡] Ahmet A. Ünal,[¶] Sergio Valencia,[¶] Florian Kronast,[¶] Leonid V. Zhigilei,[§,∇] and Rantej Bali*,[†]

†Helmholtz-Zentrum Dresden-Rossendorf, Institut für Ionenstrahlphysik und Materialforschung, Bautzner Landstrasse 400, D-01328 Dresden, Germany

‡Technische Universität Dresden, Helmholtzstrasse 10, 01069 Dresden, Germany

§Department of Materials Science and Engineering, University of Virginia, 395 McCormick Road, Charlottesville, Virginia 22904-4745, United States

∥Instituto Superior Techico (IST/UTL), ICEMS, Av. Rovisco Pais 1, 1049-100 Lisboa, Portugal

⊥Institute for Physics of Microstructures of RAS, GSP 105, 603950 Nizhny Novgorod, Russia

#Paul Scherrer Institute, 5232 Villigen PSI, Switzerland

¶Helmholtz-Zentrum Berlin für Materialien und Energie, Albert-Einstein-Strasse 15, D-12489 Berlin, Germany

∇Department of Modern Functional Materials, ITMO University, 49 Kronverksky pr., St. Petersburg 197101, Russia

S *Supporting Information*

ABSTRACT: Manipulation of magnetism using laser light is considered as a key to the advancement of data storage technologies. Until now, most approaches seek to optically switch the direction of magnetization rather than to reversibly manipulate the ferromagnetism itself. Here, we use ~100 fs laser pulses to reversibly switch ferromagnetic ordering on and off by exploiting a chemical order−disorder phase transition in $Fe_{60}Al_{40}$, from the B2 to the A2 structure and vice versa. A single laser pulse above a threshold fluence causes nonferromagnetic B2 $Fe_{60}Al_{40}$ to disorder and form the ferromagnetic A2 structure. Subsequent laser pulsing below the threshold reverses the surface to B2 $Fe_{60}Al_{40}$, erasing the laser-induced ferromagnetism. Simulations reveal that the order−disorder transition is regulated by the extent of surface supercooling; above the threshold for complete melting throughout the film thickness, the liquid phase can be deeply undercooled before solidification. As a result, the vacancy diffusion in the resolidified region is limited and the region is trapped in the metastable chemically disordered state. Laser pulsing below the threshold forms a limited supercooled surface region that solidifies at sufficiently high temperatures, enabling diffusion-assisted reordering. This demonstrates that ultrafast lasers can achieve subtle atomic rearrangements in bimetallic alloys in a reversible and nonvolatile fashion.

KEYWORDS: magneto-optical devices, data storage, phase transitions, fs laser modifications, supercooling, order−disorder transitions
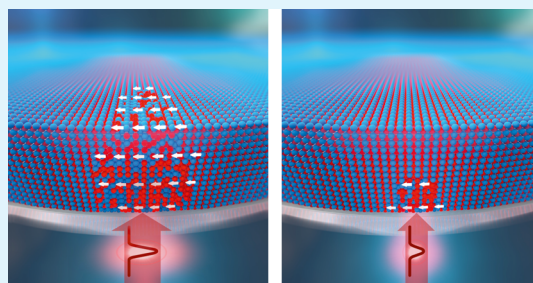
INTRODUCTION

The reversible manipulation of material properties by laser pulses is central to technologies employed on an everyday basis, such as in rewriteable (rw) optical data storage devices. In recent years, there is a thrust toward integrating optical and magnetic data storage, attempting to simultaneously exploit the ultrafast timescales of laser pulsing and the density of magnetic recording. This challenge is currently being approached via optical magnetization reversal[1−4] and heat-assisted magnetic recording.[5−8] The above phenomena do not involve changes to the intrinsic magnetic properties, that is, the saturation magnetization (M_s) of the material remains unchanged during the switching process. From a practical point of view, the detection of rw magnets within nonmagnetic matrices will show much stronger demarcations in comparison to the status quo

where data bits are recorded in terms of the magnetic stray field direction. Furthermore, laser-assisted on/off switching of ferromagnets has the potential to enable the incorporation of an optical lever to spin-transport devices.

Here, we show strong laser-induced reversible variations of M_s in a B2 $Fe_{60}Al_{40}$ alloy. This alloy is a member of a wider class of alloys of the form $Fe_{1−x}A_x$, where A = Al, V, and Rh, which are nonferromagnetic in the B2 structure but transform to strong ferromagnets via disordering to the A2 structure.[9−13] Disordering implies the exchange of site occupancies between a small fraction of the Fe and A atoms. In B2 $Fe_{60}Al_{40}$, the (001)

planes consist purely of Fe atoms, whereas the (002) planes consist primarily of Al and the remaining Fe atoms. This structure possesses the lowest Fe−Fe coordination and is known to be paramagnetic. Disordering of the B2 structure by randomly exchanging Fe and Al site occupancies, forming antisite defects, increases the average number of Fe−Fe nearest neighbors from 2.7 in the B2 structure to 4.8 in A2. Associated with the B2 → A2 transition is a slight increase in the lattice parameter, which along with the increased number of Fe−Fe nearest neighbors, may play a role in inducing ferromagnetism. Disordering can be generated locally, for example, by using a highly focused noble gas ion beam,[14] to selectively magnetize nanoscale regions of desired geometries.[15]

Although ion-induced reordering is possible in certain disordered alloys,[16] the viability of reversible order−disorder switching has not been demonstrated. Laser pulses are currently used to induce amorphous−crystalline transitions via rapid quenching, to reversibly control surface reflectivity of chalcogenide systems.[17] We demonstrate here a laser-assisted order−disorder transition via supercooling that switches on and off an intrinsic material property, while preserving the crystallinity of the system.

■ EXPERIMENT

To study the influence of laser pulses on the magnetization of B2 $Fe_{60}Al_{40}$, thin films were prepared on transparent MgO substrates. Thin films were prepared using magnetron sputtering of a target of the same composition in Ar atmosphere, while holding the substrate at room temperature. The as-deposited $Fe_{60}Al_{40}$ films are of the disordered A2 structure and are ordered to B2 via annealing at 773 K in vacuum. Details of the thin-film growth and characterization of the ordered structure have been published elsewhere.[18] Laser irradiation experiments were performed at the spin-resolved photoemission electron microscope (SPEEM) at the BESSY II storage ring in Berlin.[19] This setup provides high-resolution magnetic imaging in combination with a titanium−sapphire laser for local laser excitation. The SPEEM was used for imaging magnetization at the $Fe_{60}Al_{40}$/vacuum surface, whereas underneath the sample, a microlens was used to focus a laser of 800 nm wavelength and ∼100 fs pulse duration to a 2 μm spot. Note that, in this geometry, the laser is incident on the MgO/$Fe_{60}Al_{40}$ interface (Figure 1). The SPEEM setup and, in particular, the geometric arrangement of laser incidence and
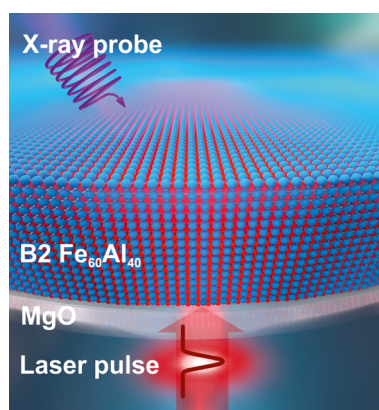
surface probing have been described in ref 20. Laser pulse irradiation was performed on B2 $Fe_{60}Al_{40}$ films of 20, 40, and 80 nm thicknesses. The laser repetition rate was 2.5 MHz, and a pulse picker was used to select single pulses or trains of defined number of pulses. Magnetic images of the laser exposed area were recorded at the L_3 resonance of Fe (707 eV), exploiting the element-specific X-ray magnetic circular dichroism.

Irradiation of a 40 nm thick B2 $Fe_{60}Al_{40}$ film by a single laser pulse at a fluence of 500 mJ cm^{-2} induces strong surface magnetic contrast (Figure 2a). The magnetic contrast is displayed as the difference of the two images recorded with circular polarization and opposite helicity, divided by their sum. The contrast sensitivity lies along the X-ray beam, with the magnetization parallel to the probe beam shown in red and antiparallel as blue. The magnetized region shows multiple domains, with some domains with lateral dimensions of 800 nm. Magnetic domains of similar sizes have been previously observed in A2 $Fe_{60}Al_{40}$.[21]

To observe the effect of low-fluence pulses, the magnetized region was irradiated with a pulse train of 10^5 pulses at 200 mJ cm^{-2}. The pulse train erases the surface magnetization induced by the first, high-fluence laser pulse. As seen in Figure 2b, the magnetization of this region is severely suppressed, and the multidomain state is erased. The 500 mJ cm^{-2} single-pulse irradiation was repeated on the same spot as above, but in the presence of a small field of +5 mT. Figure 2c shows that the field forces the formation of a single magnetic domain. The area with the single domain was irradiated with 10^4 pulses at 200 mJ cm^{-2}, again leading to the suppression of the magnetization (Figure 2d).

The process was repeated under varying conditions for optimization. Figure 2e shows B2 $Fe_{60}Al_{40}$ magnetized by a single 400 mJ cm^{-2} pulse irradiation under a magnetic field of −15 mT, which induces a single domain of strong magnetization. Finally, in Figure 2f, instead of a pulse train, the spot was irradiated with a single pulse at 200 mJ cm^{-2}. The single low-fluence pulse significantly suppresses the surface magnetization, by 40% on average in the case of 40 nm thick $Fe_{60}Al_{40}$.

To reveal the dependence of the magnetic contrast on the fluence in the single-pulse regime, the initial B2 $Fe_{60}Al_{40}$ film was irradiated at fluences increased in steps and the induced magnetic contrast was measured after each pulse. A magnetic field of +15 mT was applied to always confine the magnetization in the single-domain state. Figure 3a shows the increase of the induced magnetization with laser fluence for 20, 40, and 80 nm thick B2 $Fe_{60}Al_{40}$ films. The SPEEM contrast, which is proportional to M_s, increases in a sigmoidal fashion with increasing fluence. Half-maximum M_s is achieved at 300, 390, and 650 mJ cm^{-2} for 20, 40, and 80 nm film thicknesses, respectively (crosses in Figure 3a) and can be considered as the effective critical thresholds for magnetic writing, as measured by surface magnetic probing.

The magnetization suppression by trains of low-fluence laser pulses is illustrated in Figure 3b. A single "write" pulse was applied at fluences of 400 mJ cm^{-2} for the 20 and 40 nm thick films and 700 mJ cm^{-2} for the 80 nm film, followed by the application of 200 mJ cm^{-2} pulses for studying erasure. The "erase" pulses were applied in logarithmic steps, that is, 10^0, 10^1...10^4, 5×10^4, and 5×10^6 pulses, and after each pulse train, the surface magnetic contrast was measured. Figure 3b illustrates the variation of the magnetic contrast signal, normalized to the contrast induced by the write pulse. For the 40 and 80 nm $Fe_{60}Al_{40}$ films, this normalized magnetization,

Figure 1. Experimental scheme. The interface between $Fe_{60}Al_{40}$ and MgO is irradiated by high-intensity ∼100 fs laser pulses. The magnetic properties of the $Fe_{60}Al_{40}$ surface are probed by an X-ray beam.

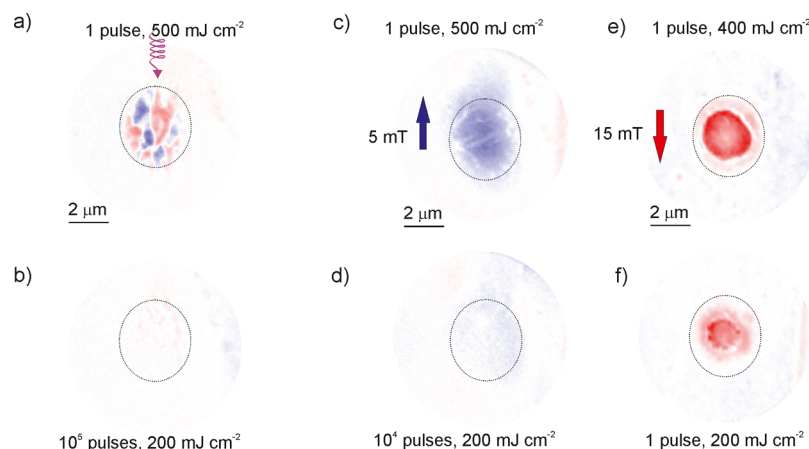**Figure 2.** Laser-assisted magnetic writing and erasing at surfaces. (a) Single pulse at 500 mJ cm^{-2} incident on a 40 nm thick B2 Fe$_{60}$Al$_{40}$ film generates a magnetic multidomain state. (b) Sample is irradiated with 10^5 pulses of the same laser, but at 200 mJ cm^{-2} per pulse, thereby erasing the multidomain state. (c) Single pulse of 500 mJ cm^{-2} is incident while a magnetic field of +5 mT is applied, generating a single domain magnet. (d) Train of 10^4 pulses at 200 mJ cm^{-2} per pulse, while retaining the magnetic field, erases the magnet. (e) Single pulse of 400 mJ cm^{-2} incident on the sample, while applying a magnetic field of −15 mT, generates a single domain magnet. (f) Significant reduction of magnetic contrast is obtained by applying a single pulse at 200 mJ cm^{-2}. The dotted ellipses outline the approximate laser-affected zone. The direction of X-ray incidence is indicated by the spiral arrow in (a). Red and blue indicate parallel and antiparallel magnetization components, respectively, with respect to the X-ray incidence.
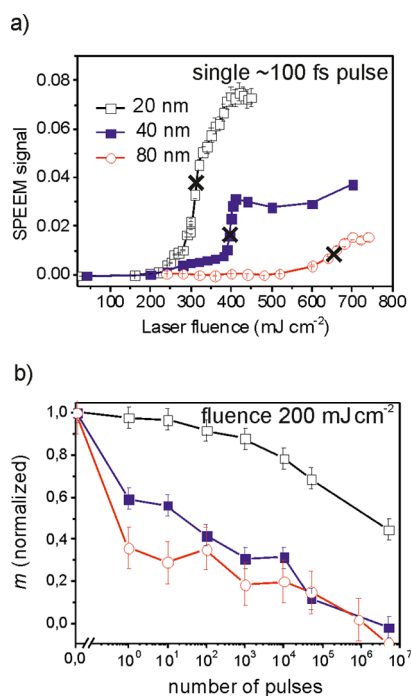

Figure 3. Magnetic response of B2 Fe$_{60}$Al$_{40}$ films to femtosecond laser irradiation. (a) Induced magnetization in terms of SPEEM contrast for single-shot irradiation of 20, 40, and 80 nm films and (b) effect of laser pulse trains of 200 mJ cm^{-2} per pulse on the normalized magnetization. The crosses in (a) indicate the fluence of the single-shot irradiation, prior to the irradiation by pulse trains in (b).

m, is suppressed strongly by the erase pulses, with 40 and 60% reductions with a single erase pulse for the 40 and 80 nm films, respectively. In comparison, for the 20 nm film, m is suppressed by 50%, but only after the application of 5×10^6 pulses.

To confirm that chemical ordering (B2 → A2 phase transition) is responsible for the laser-induced magnetic writing, an ex situ experiment was performed. The surface of a 40 nm thick B2 Fe$_{60}$Al$_{40}$ film was irradiated in air using a Q-switched Nd:YAG laser of 355 nm wavelength. The pulse width was 5 ns, and 10^5 pulses at 500 mJ cm^{-2} fluence were applied. A large laser-affected zone of ∼300 μm diameter is obtained, with an ablated region at the center. A magneto-optic Kerr effect was used to detect induced magnetization. A large induced magnetization is observed in the annular region surrounding the ablated spot. For structure analysis, a cross-sectional transmission electron microscopy (TEM) lamella was extracted from the magnetized region, away from the ablated zone, by in situ lift-out using a focused ion beam tool. The bright-field image (see Supporting Information) shows that the film possesses a flat topography, and intermixing at the film–substrate interface is negligible. Selected-area electron diffraction confirms the absence of any superstructure reflections, viz., 100, 111, and 210 associated with the B2 Fe$_{60}$Al$_{40}$ structure, thereby proving that the laser-irradiated region is fully disordered. Furthermore, no secondary phases are detected. Because the disordered structure is known to be ferromagnetic,[9−11,14,15] it is clear that the observed laser-induced magnetization occurs purely due to the formation of A2 Fe$_{60}$Al$_{40}$. The laser-assisted B2 → A2 transition is consistent with the decreasing surface magnetization with increasing film thicknesses seen in Figure 3a, with the degree of disorder decaying with the distance from the point of laser incidence.

Despite the differences in laser parameters and experimental geometry, the magnetized state is achieved in both the ex situ and in situ experiments, showing that laser pulses over a broad parameter range are effective in disordering B2 Fe$_{60}$Al$_{40}$ thin films. The reverse effect, however, has only been observed in the in situ experiment, where the laser is incident at the film–substrate interface and the magnetization is probed at the surface.

■ SIMULATION RESULTS AND DISCUSSION

To provide a clear understanding of the conditions that control the structural disordering and reordering responsible for the rw magnetization of thin films, a series of simulations of laser-induced phase transformations in Fe$_{60}$Al$_{40}$ films deposited on MgO substrates were performed. The simulations were done with a continuum level model accounting for the laser
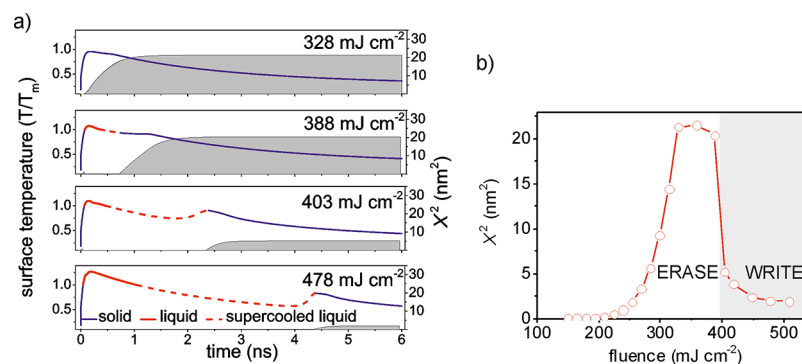
Figure 4. Computational predictions of the continuum level model of laser-induced phase transformations. (a) Temporal evolution of the surface temperature and the mean square displacement of vacancies (X^2) in the center of irradiated spot. The simulations were performed for 40 nm thick $Fe_{60}Al_{40}$ films irradiated by 100 fs laser pulses at different fluences. The evolution of surface temperature is illustrated by the lines, where the solid blue, solid red, and dashed red lines represent the phase states of solid, liquid, and supercooled liquid, respectively. The cumulative mean square displacement of vacancies in the solidified surface region, X^2, is indicated by the gray zone. (b) Dependence of the saturation level of X^2 on laser fluence. Fluence ranges suitable for magnetic writing and erasing, as suggested by the vacancy diffusion length, are marked.

excitation of the conduction band electrons, electron–phonon equilibrium, heat transfer, and the kinetics of melting and solidification (see Methods). The model accounts for the temperature dependencies of the material properties, and the irradiation conditions similar to those used in the experiments and illustrated in Figure 1 are reproduced in the simulations. The laser pulse is focused on a 2 μm spot at the film–substrate interface and is assumed to have a Gaussian intensity distribution. Although the calculations were performed for all three film thicknesses, in the discussion below, we focus on the 40 nm thick $Fe_{60}Al_{40}$ films for which the laser-induced magnetic write/erase has been found to be most pronounced.

As the first step, we performed a series of simulations for a broad range of laser fluences and identified incident fluence thresholds for the onset of melting at the $Fe_{60}Al_{40}$/MgO interface (173 mJ cm^{-2}), the emergence of the second melting region on the top surface of the film (357 mJ cm^{-2}), and the complete melting throughout the thickness of the film when the two melting fronts propagating from the film–substrate interface and the top surface merge together (394 mJ cm^{-2}). It can be expected that rapid solidification of the temporally molten part of the film produces a disordered metastable A2 phase. The metastable phase can then undergo the A2 → B2 ordering phase transition upon further cooling of the solidified material. Because the atomic rearrangements responsible for the ordering phase transition proceed through the vacancy diffusion mechanism and SPEEM measurements are sensitive to magnetization in a thin surface layer of the irradiated films, we evaluate the mean square displacement of vacancies, X^2, in the surface region located at the center of the laser spot from the time of complete solidification of this region until the cooling brings the vacancy diffusion to a halt. Although the temperature dependence of the thermodynamic driving force for the ordering phase transition does not allow us to quantitatively link the magnitude of X^2 to the kinetics of the phase transition, it still provides an instructive measure of the extent of atomic rearrangements involved in the transformation to the chemically ordered state.

The temporal evolution of the surface temperature at the center of the laser spot is illustrated in Figure 4a for four representative simulations. The color of the curves represents the phase of the material, with blue and red colors corresponding to solid and liquid phases, respectively. The

supercooling of the molten alloy below T_m is depicted by the dashed red curves (a single value of $T_m = 1660$ K taken between the solidus and liquidus of the alloy, 1630 and 1680 K,[22] is used here to simplify the discussion and the calculations), and the cumulative mean square displacements of vacancies, X^2, are shown by gray zones. At 328 mJ cm^{-2}, below the onset of surface melting, a rapid heating of the surface region almost to T_m results in a sharp increase of X^2. The following cooling, however, slows down the vacancy diffusion until it becomes negligible as the surface temperature drops below ~0.7T_m (1160 K), as reflected by the saturation of X^2. When the laser fluence is increased to 388 mJ cm^{-2}, the surface temperature exceeds T_m, leading to a transient melting of a thin surface layer of the film. The two melting fronts, propagating from the surface and film–substrate interface, do not merge in this simulation, and a rapid regrowth of the crystalline part of the film results in solidification of the surface region at a very mild supercooling of the melt (the dashed segment of the red curve in Figure 4a is short). The relatively high surface temperature at the time of the surface resolidification ensures that active vacancy diffusion can take place during further cooling of the surface, yielding the saturation level of X^2 similar to that observed at 328 mJ cm^{-2}.

Above the threshold for complete melting throughout the thickness of the film, the possibility for rapid regrowth of the crystalline part of the thin film is excluded and the solidification of the molten region can only proceed via lateral propagation of the solidification front from the periphery of the molten region to the center of the laser spot. Given the relatively large lateral size of the molten region (controlled by the size of the laser spot) and the limited velocity of the solidification front ($\leq$130 m/s, see Methods), the solidification process takes longer time and allows for much stronger supercooling of the molten material in the central part of the laser spot. In particular, a sharp increase of the solidification time from 740 ps at 388 mJ cm^{-2} to 2.4 ns at 403 mJ cm^{-2} leads to the decrease of the surface temperature at the time of complete solidification from 0.93 to 0.91T_m. Moreover, the value 0.91T_m corresponds to a maximum produced by a temperature spike appearing because of a local release of the latent heat of solidification, which quickly dissipates due to the large local temperature gradient near the freshly solidified surface. The low temperature in the resolidified region severely constrains the vacancy diffusion, as
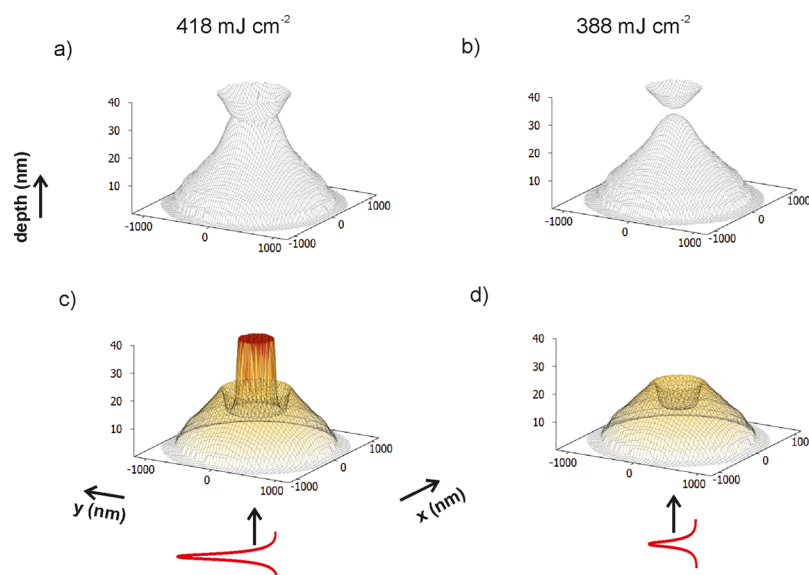
Figure 5. Rendering of the furthest extent of the melting front and corresponding effect on the magnetization. The $Fe_{40}Al_{40}$ film is irradiated at laser fluences of 418 mJ cm^{-2} in (a,c) and 388 mJ cm^{-2} in (b,d). (a,b) The maximum extent of the melting fronts during single-pulse laser irradiation of given fluences. (c,d) Spatial distribution of the induced magnetization, by considering a threshold value of the cumulative vacancy mean square displacement in the solidified material, $X^2 = 11$ nm^2. The color scale in (c,d) indicates the depth under the film−vacuum surface of the 40 nm thick film, with darker shades used closer to the surface.

indicated by the X^2 profile calculated for 403 mJ cm^{-2}, and leads to the saturation value of X^2 that is about four times smaller than that predicted for 388 mJ cm^{-2}. Further increase of the laser fluence results in longer times for solidification of the central part of the laser spots and further suppression of the vacancy diffusion. In particular, when the fluence is increased from 403 to 478 mJ cm^{-2}, the surface temperature at the time of solidification drops from $0.91T_m$ to $0.83T_m$ and the saturation level of X^2 decreases down to the values that preclude possibility of any significant atomic rearrangements after the surface resolidification, as illustrated in the bottom panel of Figure 4a.

To further illustrate the effect of the laser fluence on vacancy diffusion, we plot in Figure 4b the X^2 as a function of fluence. Below the threshold for inducing the second melting front from the surface of the film, the vacancy diffusion length increases exponentially with the laser fluence. After the onset of surface melting, X^2 saturates at an almost constant level, with only a slight decrease with the increase of laser fluence due to stronger supercooling at the point of surface resolidification. Above the threshold for complete melting, the time needed for the resolidification of the central part of the laser spot rises sharply and, as a result, a much stronger supercooling is produced prior to the resolidification. The strong supercooling, in turn, limits the vacancy diffusion during the cooling of the resolidified surface and reduces the likelihood of A2 → B2 reordering that requires atomic rearrangements. The chemically disordered state and magnetization, thus, are expected to remain in the central part of the laser spot after rapid quenching down to the room temperature.

Below the threshold for the complete melting of the film, the vacancy diffusion can be sufficiently active to allow for the ordering transition. Indeed, the maximum $X^2 \approx 21.5$ nm^2 in Figure 4b corresponds to $\sim$320 vacancy jumps. Taking into account that a typical concentration of vacancies generated in rapid nonequilibrium solidification of metals is on the order of 10^{-3} of lattice sites,[23] we can estimate that approximately 32%

of atoms change their positions because of the vacancy diffusion. Although it is not possible to quantitatively relate the total number of vacancy jumps during the cooling process to the relative fractions of the equilibrium B2 and metastable A2 phases generated by the laser irradiation, the above estimation does suggest that a substantial reordering may take place even in a single laser pulse irradiation. This conclusion is in agreement with experimental results shown in Figures 2f and 3b, which demonstrate a substantial magnetization decrease after irradiation of 40 and 80 nm films with a single laser pulse. Experimental observations of vacancies in $Fe_{60}Al_{40}$ films have been reported in ref 24.

The generation of ferromagnetic domains formed by laser irradiation performed in the absence of magnetic fields (Figure 2a) is in line with the predicted melting and resolidification scheme. Resolidification is expected to proceed via regrowth of the solid parts of the film, heterogeneous nucleation of new crystallites at the film−substrate interface, and in the case of sufficiently deep supercooling, for instance, $\sim 0.6T_m$ for a 478 mJ cm^{-2} single pulse (Figure 4a), via the homogeneous nucleation of crystallites within the melt. As resolidification proceeds, latent heat of melting is released at grain growth sites, resulting in a laterally inhomogeneous temperature distribution over the laser-affected zone. The temperature inhomogeneity may persist as the system cools to the Curie temperature (T_c), causing a spatially inhomogeneous re-entry of ferromagnetism. Regions at a local temperature of $T_c - \Delta T$ are magnetized, and their stray fields drive the local orientations of magnetic moments in their vicinity that are still at $T_c + \Delta T$, thereby inducing magnetic domains as seen in Figure 2a. The formation of magnetic domains is avoided by applying a small magnetic field during irradiation that is sufficient to override inhomogeneous stray fields and generate the single magnetic domains shown in Figure 2c,e.

To obtain an estimate of the spatial distribution of the induced magnetization, it is necessary to quantitatively relate the simulated X^2 distribution to the experimentally observed m.

The first step is to relate X^2 to the degree of the B2 $\leftrightarrow$ A2 transition, and the next step is to relate the degree of chemical disordering to m. In the second step, the correlation between the degree of disordering and the induced m is known to be in the form of an s-shaped curve,[18] which is not dissimilar to the observed laser fluence-m relationship seen in Figure 3a. However, the relationship between X^2 and the degree of chemical disordering in $Fe_{60}Al_{40}$ is not unique and depends on the thermal history of the alloy. Moreover, the time–temperature–transformation (TTT) diagram for the B2 $\leftrightarrow$ A2 transition, needed for making a quantitative connection between the temperature evolution and the degree of the phase transformation, is not available.

In the absence of TTT curves, we consider our observations: first, as seen in Figure 4b, just below the threshold fluence of $\sim$400 mJ cm^{-2}, X^2 exhibits a sharp drop from $\sim$20 to $\sim$5 nm^2, which we assume is coincident with a sharply increased m. Second, it is seen that above the threshold, a postmelting $X^2 \approx$ 2 nm^2 does not suppress m. In the first approximation, we assume that for $X^2 = 20$ nm^2, the material is fully ordered ($m = 0$) and at $X^2 = 2$ nm^2, it remains fully disordered ($m = 1$). We fix the m-spatial distribution to the halfway point of the above limiting values, that is, $X^2 = 11$ nm^2. This implies that the induced m is confined to a region within a surface defined by $X^2 = 11$ nm^2.

As a cautionary note, because the link between X^2 and disorder is dependent on the thermal history, the above limiting values can vary significantly depending on experimental conditions. Nonetheless, for any given case, a comparison of the X^2 distributions above and below the threshold fluence sheds light on the single-pulse m writing and erasing. In particular, the shape of the region undergoing transient melting and rapid resolidification and the concomitant X^2 distribution provide a qualitative picture of the spatial confinement of the disordering and reordering processes at the film surface. Figure 5a,b shows the spatial extent of the melting process at laser fluences of 388 and 418 mJ cm^{-2}, respectively. The corresponding $X^2 = 11$ nm^2 surfaces for the two fluences are shown in Figure 5c,d, respectively.

As seen in Figure 5a, at a fluence of 418 mJ cm^{-2}, the melting fronts emergent from the film surface and the interface coalesce, leading to the appearance of a melt-through region. The solidification of this region proceeds through the propagation of the solidification front and, as explained above, takes several nanoseconds. The temperature of the molten region continues to decrease and by the time of complete solidification becomes too low for atomic rearrangements needed for full chemical reordering. Figure 5c shows the corresponding limiting m surface, as obtained by plotting $X^2 = 11$ nm^2. A magnetized region of approximately 500 nm in diameter is predicted at the surface. At the MgO/film interface, the predicted magnetized region is approximately the size of the laser spot. The size of the surface magnetized region increases with increasing laser fluence.

At a fluence of 388 mJ cm^{-2}, which is just below the threshold fluence, the two melting fronts propagating from the MgO/film interface and the film top surface remain separated (Figure 5b). After the temperature drops below the melting point, the melting fronts propagate vertically and the film rapidly resolidifies. The temperature at the end of solidification remains high, which enables active vacancy diffusion. The diffusional atomic rearrangements result in the transformation of the metastable disordered A2 structure formed in the

transiently melted and resolidified parts of the film into the equilibrium B2 structure, thus erasing the surface magnetization, as can be seen from Figure 5d.

As seen in the visualizations in Figure 5, a residual magnetization can occur in the bottom 20 nm of the film, even for low-fluence laser pulses. The onset of interfacial melting is $\sim$180 mJ cm^{-2} for all film thicknesses, and a 200 mJ cm^{-2} pulse leads to transient melting and formation of residual disorder at the MgO/film interface. This is consistent with the observations in Figure 3b, where single-pulse erasure is not observed in 20 nm thick $Fe_{60}Al_{40}$. Laser irradiation by up to $\sim$10^6 pulses tends to reorder the upper layers of the film, nevertheless the residual magnetization persists. Because the depth of SPEEM probing is limited to a depth of $\sim$10 nm, the presence of this magnetized layer is detectable only in the case of 20 nm film. Rewritable magnetization, therefore, is observed for film thicknesses above 20 nm.

■ CONCLUSIONS

The proof of principle for laser-induced on/off switching of ferromagnetism driven by a disorder–order transition has been demonstrated on B2 alloy thin films. Simulations reveal the crucial role played by supercooling of the transiently melted region in manifesting the disorder–order transition. The process is repeatable-laser pulses of fluences above the writing threshold have been applied up to 10 times at the same spot without the appearance of damage to the film. Repeatability can be limited by ablation of the material or by contamination during the laser irradiation process; factors that can be avoided by an appropriate protective top layer, such as MgO. Engineering the substrate heat conductivity and the inclusion of a buffer and cap layers should be explored for increasing the maximum level of supercooling before the resolidification to control diffusion and reordering, and to achieve optimized laser-assisted reversible property changes. The concept of laser-induced rw magnetization may be applicable to other materials that exhibit order–disorder transitions. Further studies on these materials may improve our understanding of femtosecond laser-induced rapid heating and cooling processes in alloys, in particular, the mechanisms and kinetics of the order–disorder transition that are still largely unexplored. The results of this study may initiate a wider search for new alloys exhibiting laser-induced reversible changes of intrinsic magnetic properties.

■ METHODS

Experiments. Details on the thin-film preparation can be found in ref 18. The PEEM experiment combined with laser irradiation is described in ref 20.

Simulations. The initial response of a $Fe_{60}Al_{40}$ film deposited on a magnesia (MgO) substrate to a short-pulse laser irradiation has been simulated with a conventional one-dimensional (1D) two-temperature model (TTM)[25] that provides a continuum level description of the laser excitation and subsequent relaxation of the conduction band electrons. The description of kinetics of melting and resolidification processes is incorporated into the model as described in ref 26. The temperature profiles and the positions of the solid–liquid interface at 750 ps, predicted in series of 1D simulations, are used as input for the two-dimensional (2D) simulations applied to investigate the lateral propagation of melting front and long-term evolution of the temperature profile affected by the lateral heat transport. Simulations are performed for computational systems consisting of 20, 40, and 80 nm $Fe_{60}Al_{40}$ films on a 1 μm thick MgO substrate. The choice of the thickness of the substrate ensures a negligible temperature change at the bottom of the substrate on the simulation timescale.

The irradiation of the target by a 100 fs laser pulse directed from the magnesia–metal interface is represented through a source term added to the TTM equation for the electron temperature. The source term accounts for the excitation of the conduction band electrons by a laser pulse with a Gaussian temporal profile and reproduces the exponential attenuation of laser intensity with depth under the surface (Beer–Lambert law), with the optical absorption depth of 15 nm of Fe at the laser wavelength of 800 nm.[27] Because of the uncertainty in the reflectivity of the $Fe_{60}Al_{40}$ alloy, the absorbed laser fluence is converted into the incident one by matching the threshold of complete melting of a 40 nm film in the experiment and modeling, which gives the value of reflectivity of 0.928. In the 2D simulations, the lateral distribution of laser fluence is described by a Gaussian profile $F(r) = F_0 \exp(-r^2/2\sigma_r^2)$, where σ_r^2 is the standard deviation related to the laser spot diameter (full width at half-maximum) as $D = \sigma_r 8\ln 2$. The spot diameter is assumed to be 2 μm, and the results of 1D simulations performed at different laser fluencies are linearly interpolated to account for the radial dependence of the laser fluence when the initial temperature distribution is built.

Because the available temperature dependencies of electron heat capacity and electron–phonon coupling accounting for the contribution from the thermal excitation from the electron states below the Fermi level are mostly limited by pure metals,[28] we use parameters for pure Fe instead of $Fe_{60}Al_{40}$ alloy.[29] Similar to ref 26, the temperature dependence of the electron thermal conductivity is approximated by the Drude model relationship, $K_e(T_e,T_l) = v^2 C_e(T_e) \tau_e(T_e,T_l)/3$, where $C_e(T_e)$ is the electron heat capacity, v^2 is the mean square velocity of the electrons contributing to the electron heat conductivity, approximated in this work as the Fermi velocity squared, v_F^2, and $\tau_e(T_e,T_l)$ is the total electron scattering time defined by the electron–electron scattering rate, $1/\tau_{e-e} = A T_e^2$, and the electron–phonon scattering rate, $1/\tau_{e-ph} = B T_l$, so that $1/\tau_e = A T_e^2 + B T_l$. The value of the coefficient A (8.9×10^5 K^{-2} s^{-1}) is estimated within the free electron model.[30] The coefficient B is described as a function of the lattice temperature, so that the experimental temperature dependences of thermal conductivity of the $Fe_{60}Al_{40}$ alloy under conditions of electron–phonon equilibrium[22,31] are reproduced in the simulations. Because in 2D simulations we do not explicitly consider the electron subsystem, the heat capacity used in the model is equal to the sum of electron and phonon heat capacities and the heat conductivity follows the experimental temperature dependence.[22,31]

According to the Fe–Al phase diagram,[22] the temperature of solid–liquid coexistence lies in the range 1630–1680 K and the single value of "melting temperature," $T_m = 1660$ K, is used to simplify the description of the melting and resolidification processes. The temperature dependence of the velocity of the liquid–crystal interface is described by the Wilson–Frenkel expression,[32] with parameters taken for the Fe(100) interface from ref 33. Because pure Fe has different melting temperatures than the $Fe_{60}Al_{40}$ alloy, the activation energy for diffusion and the heat of fusion are renormalized based on the T_m of the alloy to ensure the same velocity of the interface at the same values of relative undercooling T/T_m:

$$V_I = V_0 \cdot \exp(-\tilde{Q} \cdot T_m/T)[1 - \exp(-\tilde{H}_f \cdot (T_m/T - 1))]$$

where V_0 is a prefactor equal to 2200 m/s, $\tilde{Q} = Q^{Fe}/k_B T_m^{Fe} = 1.23$ is the reduced activation energy for diffusion, and $\tilde{H}_f = H_f^{Fe}/k_B T_m^{Fe} = 0.884$ is the reduced heat of fusion. To account for the fast homogeneous melting of the superheated solid, the regions of the target where the lattice temperature exceeds $1.3T_m$ (ref 34) are set to undergo instantaneous melting. The lattice heat capacity of the alloy is assumed to be equal to 3R and is calculated based on the lattice parameter 2.898 Å (ref 35) of B2 $Fe_{60}Al_{40}$, which gives 3.4×10^6 J m^{-3} K^{-1}. The heat of fusion is estimated as a weighted average of values for Al and Fe based on the concentration in the alloy, which gives 1.7×10^9 J m^{-3}.

The heat capacity of magnesia is assumed to be 3.3×10^6 J m^{-3} K^{-1} (ref 36), and the thermal conductivity is fitted as $K(T) = 10\,700/(T - 46.0)$ [W K^{-1} m^{-1}] based on values provided in ref 37. Because the value of interfacial thermal conductance depends not only on the materials in the contact but also on the method of the film deposition and cannot be evaluated without direct measurement, we assumed it to be 10^8 W m^{-2} K^{-1}, a typical value from the experimentally measured range of 10^7 to 10^9 W m^{-2} K^{-1} (refs 38–41).

■ ASSOCIATED CONTENT

ⓢ Supporting Information

The Supporting Information is available free of charge on the ACS Publications website at DOI: 10.1021/acsami.8b01190.

Results of structural analysis using TEM, as well as additional simulation results included (PDF)

■ AUTHOR INFORMATION

Corresponding Author

*E-mail: r.bali@hzdr.de.

ORCID ⓘ

Jonathan Ehrler: 0000-0002-5187-2808
Sergio Valencia: 0000-0002-3912-5797
Rantej Bali: 0000-0002-5325-4018

Author Contributions

R.B. conceived the project in discussions with N.I.P. and F.K. J.E., S.W., and V.L. performed SPEEM measurements. M.H. and M.V.S. performed simulations. A.A.Ü., S.V., and F.K. provided beamline support. J.E., V.L., and S.C. prepared thin-film samples. N.I.P. performed ex situ tests. R.H. performed TEM analysis. K.P., J.L., and J.F. supervised the experimental work. L.V.Z. supervised the simulations. All co-authors contributed to writing the manuscript. R.B. coordinated the overall project.

Notes

The authors declare no competing financial interest.

■ REFERENCES

(1) Guyader, L. L.; Savoini, M.; El Moussaoui, S.; Buzzi, M.; Tsukamoto, A.; Itoh, A.; Kirilyuk, A.; Rasing, T.; Kimel, A. V.; Nolting, F. Nanoscale sub-100 picosecond all-optical magnetization switching in GdFeCo microstructures. *Nat. Commun.* **2015**, *6*, 5839.

(2) Kimel, A. V.; Kirilyuk, A.; Usachev, P. A.; Pisarev, R. V.; Balbashov, A. M.; Rasing, T. Ultrafast non-thermal control of magnetization by instantaneous photomagnetic pulses. *Nature* **2005**, *435*, 655–657.

(3) Lambert, C.-H.; Mangin, S.; Varaprasad, B. S. D. C. S.; Takahashi, Y. K.; Hehn, M.; Cinchetti, M.; Malinowski, G.; Hono, K.; Fainman, Y.; Aeschlimann, M.; Fullerton, E. E. All-optical control of ferromagnetic thin films and nanostructures. *Science* **2014**, *345*, 1337–1340.

(4) Stupakiewicz, A.; Szerenos, K.; Afanasiev, D.; Kirilyuk, A.; Kimel, A. V. Ultrafast nonthermal photo-magnetic recording in a transparent medium. *Nature* **2017**, *542*, 71–74.

(5) Stipe, B. C.; Strand, T. C.; Poon, C. C.; Balamane, H.; Boone, T. D.; Katine, J. A.; Li, J.-L.; Rawat, V.; Nemoto, H.; Hirotsune, A.; Hellwig, O.; Ruiz, R.; Dobisz, E.; Kercher, D. S.; Robertson, N.; Albrecht, T. R.; Terris, B. D. Magnetic recording at 1.5 Pb m^{-2} using an integrated plasmonic antenna. *Nat. Photonics* **2010**, *4*, 484–488.

(6) Saga, H.; Nemoto, H.; Sukeda, H.; Takahashi, M. New recording method combining thermo-magnetic writing and flux detection. *Jpn. J. Appl. Phys.* **1999**, *38*, 1839−1840.

(7) McDaniel, T. W. Ultimate limits to thermally assisted magnetic recording. *J. Phys.: Condens. Matter* **2005**, *17*, R315−R332.

(8) Kryder, M. H.; Gage, E. C.; McDaniel, T. W.; Challener, W. A.; Rottmayer, R. E.; Ju, G.; Hsia, Y.-T.; Erden, M. F. Heat assisted magnetic recording. *Proc. IEEE* **2008**, *96*, 1810−1835.

(9) Menéndez, E.; Liedke, M. O.; Fassbender, J.; Gemming, T.; Weber, A.; Heyderman, L. J.; Rao, K. V.; Deevi, S. C.; Suriñach, S.; Baró, M. D.; Sort, J.; Nogués, J. Nanostructures Direct Magnetic Patterning due to the Generation of Ferromagnetism by Selective Ion Irradiation of Paramagnetic FeAl Alloys. *Small* **2009**, *5*, 229−234.

(10) Beck, P. A. Some recent results on magnetism in alloys. *Metall. Mater. Trans. B* **1971**, *2*, 2015−2024.

(11) Huffman, G. P.; Fisher, R. M. Mössbauer Studies of Ordered and Cold-Worked Fe−Al Alloys Containing 30 to 50 at. % Aluminum. *J. Appl. Phys.* **1967**, *38*, 735−742.

(12) Krause, J. C.; Schaf, J.; da Costa, M. I., Jr.; Paduani, C. Effect of composition and short-range order on the magnetic moments of Fe in $Fe_{1−x}V_x$ alloys. *Phys. Rev. B: Condens. Matter Mater. Phys.* **2000**, *61*, 6196−6204.

(13) Heidarian, A.; Bali, R.; Grenzer, J.; Wilhelm, R. A.; Heller, R.; Yildirim, O.; Lindner, J.; Potzger, K. Tuning the antiferromagnetic to ferromagnetic phase transition in FeRh thin films by means of low-energy/low fluence ion irradiation. *Nucl. Instrum. Methods Phys. Res., Sect. B* **2015**, *358*, 251−254.

(14) Cybart, S. A.; Bali, R.; Hlawacek, G.; Röder, F.; Fassbender, J. Focused Helium and Neon Ion Beam Modification of High-TC Superconductors and Magnetic Materials, in Helium Ion Microscopy. In *Helium Ion Microscopy*; Hlawacek, G., Gölzhäuser, A., Eds.; Springer International Publishing, 2016.

(15) Röder, F.; Hlawacek, G.; Wintz, S.; Hübner, R.; Bischoff, L.; Lichte, H.; Potzger, K.; Lindner, J.; Fassbender, J.; Bali, R. Direct Depth- and Lateral- Imaging of Nanoscale Magnets Generated by Ion Impact. *Sci. Rep.* **2015**, *5*, 16786.

(16) Bernas, H.; Attané, J.-P.; Heinig, K.-H.; Halley, D.; Ravelosona, D.; Marty, A.; Auric, P.; Chappert, C.; Samson, Y. Ordering Intermetallic Alloys by Ion Irradiation: A Way to Tailor Magnetic Media. *Phys. Rev. Lett.* **2003**, *91*, 077203.

(17) Wuttig, M.; Yamada, N. Phase change materials for rewriteable data storage. *Nat. Mater.* **2007**, *6*, 824−832.

(18) Bali, R.; Wintz, S.; Meutzner, F.; Hübner, R.; Boucher, R.; Ünal, A. A.; Valencia, S.; Neudert, A.; Potzger, K.; Bauch, J.; Kronast, F.; Facsko, S.; Lindner, J.; Fassbender, J. Printing Nearly-Discrete Magnetic Patterns Using Chemical Disorder Induced Ferromagnetism. *Nano Lett.* **2014**, *14*, 435−441.

(19) Kronast, F.; Molina, S. V. SPEEM: The photoemission microscope at the dedicated microfocus PGM beamline UE49-PGMa at BESSY II. *J. Large Scale Res. Facil.* **2016**, *2*, A90.

(20) Gierster, L.; Pape, L.; Ünal, A. A.; Kronast, F. A sample holder with integrated laser optics for an ELMITEC photoemission electron microscope. *Rev. Sci. Instrum.* **2015**, *86*, 023702.

(21) Fassbender, J.; Liedke, M. O.; Strache, T.; Möller, W.; Menéndez, E.; Sort, J.; Rao, K. V.; Deevi, S. C.; Nogués, J. Ion mass dependence of irradiation-induced local creation of ferromagnetism in $Fe_{60}Al_{40}$ alloys. *Phys. Rev. B: Condens. Matter Mater. Phys.* **2008**, *77*, 174430.

(22) Ruan, Y.; Yan, N.; Zhu, H. Z.; Zhou, K.; Wei, B. Thermal performance determination of binary Fe-Al alloys at elevated temperatures. *J. Alloys Compd.* **2017**, *701*, 676−681.

(23) Lin, Z.; Johnson, R. A.; Zhigilei, L. V. Computational Study of the Generation of Crystal Defects in A BCC Metal Target Irradiated by Short Laser Pulses. *Phys. Rev. B: Condens. Matter Mater. Phys.* **2008**, *77*, 214108.

(24) Liedke, M. O.; Anwand, W.; Bali, R.; Cornelius, S.; Butterling, M.; Trinh, T. T.; Wagner, A.; Salamon, S.; Walecki, D.; Smekhova, A.; Wende, H.; Potzger, K. Open volume defects and magnetic phase transition in $Fe_{60}Al_{40}$ transition metal aluminide. *J. Appl. Phys.* **2015**, *117*, 163908.

(25) Anisimov, S. I.; Kapeliovich, B. L.; Perel'man, T. L. Electron emission from metal surfaces exposed to ultrashort laser pulses. *J. Exp. Theor. Phys.* **1974**, *39*, 375−377.

(26) Sedao, X.; Shugaev, M. V.; Wu, C.; Douillard, T.; Esnouf, C.; Maurice, C.; Reynaud, S.; Pigeon, F.; Garrelie, F.; Zhigilei, L. V.; Colombier, J.-P. Growth Twinning and Generation of High-Frequency Surface Nanostructures in Ultrafast Laser-Induced Transient Melting and Resolidification. *ACS Nano* **2016**, *10*, 6995−7007.

(27) Palik, E. D. *Handbook of Optical Constants of Solids*; Academic Press: New York, 1998.

(28) Lin, Z.; Zhigilei, L. V.; Celli, V. Electron-phonon coupling and electron heat capacity of metals under conditions of strong electron-phonon nonequilibrium. *Phys. Rev. B: Condens. Matter Mater. Phys.* **2008**, *77*, 075133.

(29) http://www.faculty.virginia.edu/CompMat/electron-phonon-coupling/Ce_Fe_BCC.dat.

(30) Groeneveld, R. H. M.; Sprik, R.; Lagendijk, A. Femtosecond spectroscopy of electron-electron and electron-phonon energy relaxation in Ag and Au. *Phys. Rev. B: Condens. Matter Mater. Phys.* **1995**, *51*, 11433−11445.

(31) Rudajevová, A.; Buriánek, J. Determination of Thermal Diffusivity and Thermal Conductivity of Fe-Al Alloys in the Concentration Range 22 to 50 at. % Al. *J. Phase Equilib.* **2001**, *22*, 560−563.

(32) Jackson, K. A. The Interface Kinetics of Crystal Growth Processes. *Interface Sci.* **2002**, *10*, 159−169.

(33) Ashkenazy, Y.; Averback, R. S. Kinetic stages in the crystallization of deeply undercooled body-centered-cubic and face-centered-cubic metals. *Acta Mater.* **2010**, *58*, 524−530.

(34) Luo, S.-N.; Ahrens, T. J.; Çağın, T.; Strachan, A.; Goddard, W. A.; Swift, D. C. Maximum superheating and undercooling: Systematics, molecular dynamics simulations, and dynamic experiments. *Phys. Rev. B: Condens. Matter Mater. Phys.* **2003**, *68*, 134206.

(35) Nogués, J.; Apiñaniz, E.; Sort, J.; Amboage, M.; d'Astuto, M.; Mathon, O.; Puzniak, R.; Fita, I.; Garitaonandia, J. S.; Suriñach, S.; Muñoz, J. S.; Baró, M. D.; Plazaola, F.; Baudelet, F. Volume expansion contribution to the magnetism of atomically disordered intermetallic alloys. *Phys. Rev. B: Condens. Matter Mater. Phys.* **2006**, *74*, 024407.

(36) Slifka, A. J.; Filla, B. J.; Phelps, J. M. Thermal Conductivity of Magnesium Oxide From Absolute, Steady-State Measurements. *J. Res. Natl. Inst. Stand. Technol.* **1998**, *103*, 357.

(37) Chase, M. W. *NIST-JANAF Thermochemical Tables*, 4th ed.; Journal of Physical and Chemical Reference Data; National Institute of Standards and Technology (NIST): Gaithersburg, MA, 1998.

(38) Hopkins, P. E.; Salaway, R. N.; Stevens, R. J.; Norris, P. M. Temperature-Dependent Thermal Boundary Conductance at Al/Al_2O_3 and Pt/Al_2O_3 interfaces. *Int. J. Thermophys.* **2007**, *28*, 947−957.

(39) Hopkins, P. E.; Phinney, L. M.; Serrano, J. R.; Beechem, T. E. Effects of surface roughness and oxide layer on the thermal boundary conductance at aluminum/silicon interfaces. *Phys. Rev. B: Condens. Matter Mater. Phys.* **2010**, *82*, 085307.

(40) Giri, A.; Foley, B. M.; Hopkins, P. E. Influence of Hot Electron Scattering and Electron−Phonon Interactions on Thermal Boundary Conductance at Metal/Nonmetal Interfaces. *J. Heat Transfer* **2014**, *136*, 092401.

(41) Cheaito, R.; Gaskins, J. T.; Caplan, M. E.; Donovan, B. F.; Foley, B. M.; Giri, A.; Duda, J. C.; Szwejkowski, C. J.; Constantin, C.; Brown-Shaklee, H. J.; Ihlefeld, J. F.; Hopkins, P. E. Thermal boundary conductance accumulation and interfacial phonon transmission: Measurements and theory. *Phys. Rev. B: Condens. Matter Mater. Phys.* **2015**, *91*, 035432.

H